

## Static and Dynamic Performance of the RBRargo<sup>3</sup> CTD

M. DEVER,<sup>a,b</sup> B. OWENS,<sup>b</sup> C. RICHARDS,<sup>c</sup> S. WIJFFELS,<sup>b</sup> A. WONG,<sup>d</sup> I. SHKVORETS,<sup>a</sup>  
M. HALVERSON,<sup>a</sup> AND G. JOHNSON<sup>a</sup>

<sup>a</sup> RBR, Ottawa, Ontario, Canada

<sup>b</sup> Woods Hole Oceanographic Institution, Woods Hole, Massachusetts

<sup>c</sup> Bedford Institute of Oceanography, Department of Fisheries and Oceans Canada, Dartmouth, Nova Scotia, Canada

<sup>d</sup> School of Oceanography, University of Washington, Seattle, Washington

(Manuscript received 28 December 2021, in final form 16 June 2022)

**ABSTRACT:** The static and dynamic performances of the RBRargo<sup>3</sup> are investigated using a combination of laboratory-based and in situ datasets from floats deployed as part of an Argo pilot program. Temperature and pressure measurements compare well to co-located reference data acquired from shipboard CTDs. Static accuracy of salinity measurements is significantly improved using 1) a time lag for temperature, 2) a quadratic pressure dependence, and 3) a unit-based calibration for each RBRargo<sup>3</sup> over its full pressure range. Long-term deployments show no significant drift in the RBRargo<sup>3</sup> accuracy. The dynamic response of the RBRargo<sup>3</sup> demonstrates the presence of two different adjustment time scales: a long-term adjustment  $O(120)$  s, driven by the temperature difference between the interior of the conductivity cell and the water, and a short-term adjustment  $O(5\text{--}10)$  s, associated to the initial exchange of heat between the water and the inner ceramic. Corrections for these effects, including dependence on profiling speed, are developed.

**KEYWORDS:** Data processing/distribution; In situ oceanic observations; Profilers, oceanic

### 1. Introduction

Diversification of conductivity–temperature–depth (CTD) instrumentation for the Argo program is crucial to avoid “points of single failure” (Roemmich et al. 2019). As an alternative CTD to the one currently used on Argo floats, the RBRargo<sup>3</sup>, manufactured by RBR Ltd., was approved for a trial phase to assess its in situ performance. Several floats equipped with the RBRargo<sup>3</sup> have thus been deployed and a task team with members from the Argo community and RBR was formed in 2020 to assess instrument accuracy across a range of ocean regimes, help improve calibrations, and develop the procedures to yield the highest data quality.

The RBRargo<sup>3</sup> conductivity cell relies on a different working principle than the SBE41CP CTD currently used on Argo floats, which relies on an electrode-based measurement of conductivity within a borosilicate glass cell through which water is actively and continuously pumped (Lueck 1990). The RBRargo<sup>3</sup>, on the other hand, uses a free-flushing, low aspect ratio conductivity cell (Fig. 1; Halverson et al. 2020b). As a result, it is important for the conductivity cell to be facing the direction of the flow to ensure the best data quality. Conductivity measurements of the seawater in the vicinity of the cell are made according to Faraday’s law of induction, using two toroidal coils—a generating coil and a receiving coil. An alternating voltage is applied to the generating coil, producing a time-varying magnetic field and thereby inducing a current in the seawater inside and surrounding the cell (Fig. 1). The induced current

loops through the seawater and passes through the center of the receiving coil, generating a secondary current. The measured current in the receiving coil is proportional to the conductivity of the seawater present in the measurement volume. As a result, any material located within the sampling volume of the conductivity cell (i.e., 15-cm-radius sphere) would impact conductivity measurements. While conductive materials would generate a positive bias in the salinity, insulating materials would lead to a negative bias in the salinity estimates.

According to the manufacturer, the static accuracy at sea level of the RBRargo<sup>3</sup> is stated to be  $\pm 0.003$  mS cm<sup>-1</sup>,  $\pm 0.002^\circ\text{C}$ , and  $\pm 1$  dbar for conductivity, temperature, and pressure, respectively. However, compressibility effects can affect the static accuracy of conductivity at high pressures, and sensor drift can degrade the static accuracy of conductivity measurements over time. The profiling nature of Argo floats also generate dynamic errors in CTD observations (Lueck and Picklo 1990; Morison et al. 1994; Johnson et al. 2007). In fact, dynamic errors emerge in CTD observations when collected from any moving platform sampling through a temperature gradient, and are proportional to the amplitude of the temperature gradient. These dynamic errors are generated by different processes linked to the physical arrangement of the sensors, the inherent response time of the sensors, and the thermal inertia of the conductivity cell.

In this study, each of these sources of error are characterized and postprocessing techniques are developed to correct these errors in order to improve the resulting data accuracy.

### 2. Theoretical framework

#### a. Static-accuracy and compressibility correction

Static accuracy of the temperature, conductivity, and pressure from the RBRargo<sup>3</sup> is determined during the calibration

 Denotes content that is immediately available upon publication as open access.

Corresponding author: M. Dever, mathieu.dever@rbr-global.com

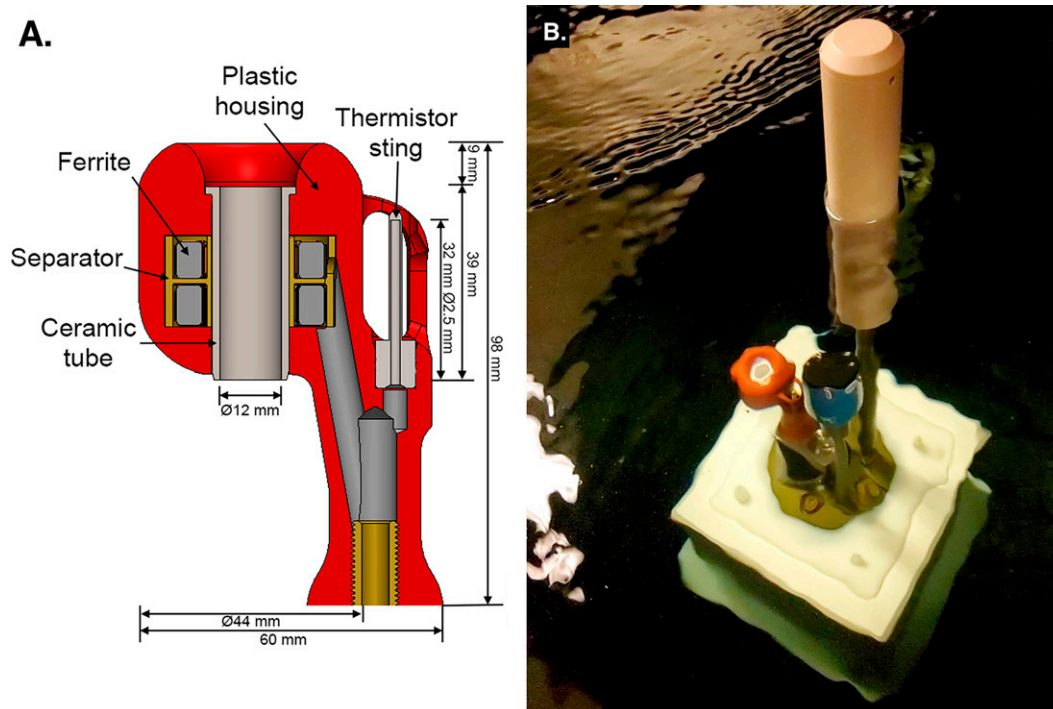


FIG. 1. (a) Schematic of the RBRargo<sup>3</sup>. (b) Photo of the RBRargo<sup>3</sup> mounted on an Argo float (manufactured by NKE instrumentation) during calibration (credits Kai Malorny).

process at RBR, and detailed on the calibration certificate provided with each RBRargo<sup>3</sup>. Temperature and conductivity are typically calibrated at atmospheric pressure, and the pressure channel is calibrated across sensor's full range (i.e., 2000 dbar). At higher pressure, however, the geometry of the conductivity cell on the RBRargo<sup>3</sup> elastically deforms. While the internal components of the conductivity cell (e.g., toroids) are protected from pressure, the change in the cell external geometry is enough to change the path of the current in the sampled seawater, introducing a pressure-dependent bias in the conductivity measurements. This compressibility error is expected to be repeatable from profile to profile and to vary for each CTD (see section 4).

#### b. Sensor stability

Each float deployed as part of the Argo program is expected to have a life expectancy of a minimum of 5 years. Sensors on board floats must therefore demonstrate not only good stability from profile to profile, but also over time scales on the order of years. Salinity drift is one of the main challenges the Argo program faces (Wong et al. 2020). Stability of salinity estimates from Argo floats can be affected by many different factors, including biofouling, biocide leakage, or degradation of the cell over time such as deformation or seawater penetration (Wong et al. 2003, 2020).

#### c. Dynamic errors and their impact on salinity estimation

The conductivity variance tends to be dominated by the temperature variance, as it is generally larger than the salinity

variance. Thus any mismatch between simultaneous temperature and conductivity measurements used to estimate salinity can generate large errors. For a profiling CTD, two types of dynamic errors affect salinity estimates: 1) a time lag between temperature and conductivity measurements and 2) a temperature difference between the fluid at the thermistor and in the measurement volume of the conductivity cell due to its larger thermal inertia (Lueck 1990; Johnson et al. 2007). Both of these dynamic errors can be observed in situ and are especially obvious when a CTD profiles through a temperature interface into a relatively homogeneous layer, which typically occur in regions of double-diffusive instability or near the base of the surface mixed layer. Figure 2 shows an example profile collected by an RBRargo<sup>3</sup>-equipped ALAMO float in the Caribbean Sea, where both the salinity and the potential density anomaly clearly exhibit artificial features at temperature interfaces (Jayne and Bogue 2017; Sanabia and Jayne 2020). The error in salinity (and potential density) has both a short time scale,  $O(5-10)$  s, seen as a high salinity/density spike near the lower boundary of the well-mixed layer, and a longer time scale  $O(120)$  s that extends over much of the mixed layers and is best visible as an artificial negative slope in the potential density as a function of pressure.

#### 1) RESPONSE TIME AND SENSOR MISALIGNMENTS

Misalignments between temperature and conductivity measurements generate errors in salinity estimates, often called "salinity spiking" (Fofonoff et al. 1974; Horne and Toole 1980; Ullman and Hebert 2014; Dever et al. 2020). This misalignment

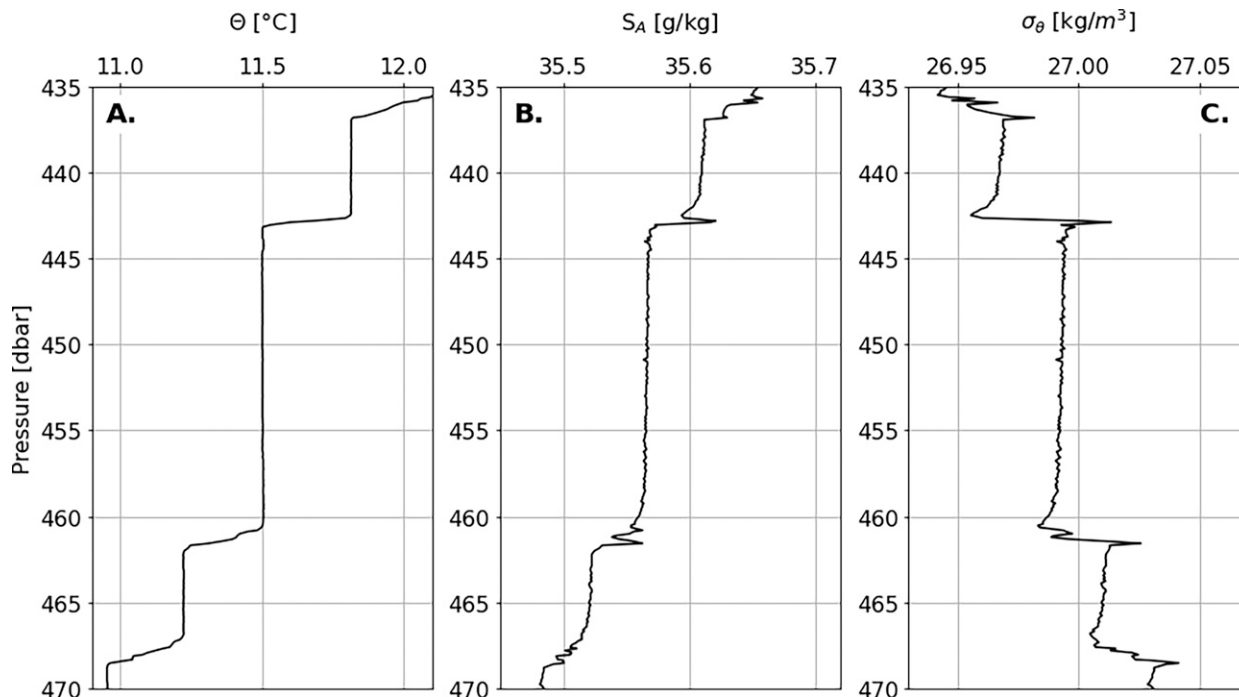


FIG. 2. Example profile from ALAMO float 9139 in the Caribbean Sea (profile 52), showing (a) the conservative temperature, (b) the absolute salinity, and (c) the potential density anomaly. The staircase structure of the water column highlights dynamic errors in both salinity and density at sharp interfaces, where both spiking and thermal inertia errors can be seen. Data courtesy of Drs Sanabia (U.S. Naval Academy) and Jayne (Woods Hole Oceanographic Institution).

is referred to as a “ $C$ – $T$  lag,” and is generated by two separate mechanisms:

- 1) The physical separation between the thermistor and the conductivity cell. As it takes time for the sampled water parcel to travel from the thermistor to the volume sampled by the conductivity cell, this “advective lag” is directly proportional to the distance between the thermistor and the conductivity cell, and is therefore dependent on the flow speed through the CTD. The RBRargo<sup>3</sup> CTD has been designed to minimize the spatial separation between conductivity and temperature, and thus the advective  $C$ – $T$  lag (see Fig. 1).
- 2) The inherent response time of the thermistor. The thermistor responds more slowly to a change in temperature than the conductivity cell which is virtually instantaneous due to the fact that it is an electrical measurement and does not rely on diffusion processes the way the thermistor does. This difference in response time introduces an apparent time lag between the temperature and conductivity, resulting in spiking in the computed salinity (Horne and Toole 1980). This  $C$ – $T$  lag is caused by the inherent properties of the thermistor and can be considered to be independent of flow speed to the first degree of approximation, thus ignoring the impact of boundary layer dynamics on sensor response.

This error can be seen in Fig. 2, with some evident salinity spiking coinciding with sharp temperature gradients, and can

be corrected by shifting the measured temperature in time using

$$T_{\text{cor}}(t) = T_{\text{meas}}(t + \Delta t), \quad (1)$$

where  $T_{\text{cor}}$  is the lagged temperature,  $T_{\text{meas}}$  is the raw temperature, and  $\Delta t$  is the prescribed lag. Other approaches than a simple time lag are sometimes considered to correct for the  $C$ – $T$  lag, such as sharpening algorithms (Fozdar et al. 1985; Bittig et al. 2014; Johnson et al. 2007). Sharpening algorithms present the advantage to further reduce the salinity spiking by reconstructing fine-scale gradients that are not captured by the sensor. However, the reliability of all these techniques depends on both the amplitude and phase reconstruction. The time-lag approach was deemed to be a good compromise between phase and amplitude reconstruction of the signal across the frequency range.

## 2) THERMAL INERTIA ERRORS

As the CTD travels through a temperature gradient, heat is exchanged between the conductivity cell and a thin boundary layer attached to the cell, which changes the temperature averaged over the conductivity measurement volume from that measured by the thermistor. Thus, the calculated salinity must use a temperature adjusted for the heat flux into the measurement volume. This is a well-known, but poorly constrained, error in CTD measurements generally, and is the focus of a research effort that has been ongoing for over three decades

(Lueck and Picklo 1990; Morison et al. 1994; Johnson et al. 2007; Martini et al. 2019; Johnson 2020; Halverson et al. 2020b). As described by Lueck (1990), the heat flux at the cell boundary will depend on the profiling speed and the difference between the cell surface temperature and  $T_{\text{cor}}$  while the thickness of the boundary layer which determines the contribution to the measurement averaged temperature will depend on the profiling speed. The surface temperature of cell will depend on the heat conduction within the cell.

While the transfer of heat into the fluid depends on the skin temperature of the cell, the change in the skin temperature will depend on the thermal conductance of the cell components. As shown in Fig. 1, the cell is constructed from materials for which the thermal conductance varies by more than a factor of 20.

In a cylindrical coordinate system, the equation describing the diffusion of heat can be written as

$$\rho C_p \frac{\partial T}{\partial t} = \frac{1}{r} \frac{\partial}{\partial r} \left( r \lambda \frac{\partial T}{\partial r} \right), \quad (2)$$

where  $\rho$  is the density of the material,  $C_p$  is the heat capacity,  $T$  is the temperature inside the conductivity cell,  $r$  is the distance from the center of the ceramic annulus (see Fig. 1), and  $\lambda$  is the thermal conductivity.

After a short time, the heat content of material near the cell boundary changes slowly, so that the left-hand side of Eq. (2) approaches zero. Thus, for longer time scales, the heat conduction into the cell can be approximated using the average thermal conductance and the difference between the temperature measured inside the cell, which must equal the heat flux through the surface boundary layer. This approximate balance leads to an expression for the temperature anomaly at long time scales:

$$T_{\text{long}} = \text{ctcoeff}(V_p) \times (T_{\text{cond}} - T_{\text{cor}}), \quad (3)$$

where  $T_{\text{long}}$  is the temperature anomaly in the sampled volume due to long-term thermal inertia,  $T_{\text{cond}}$  is the internal temperature of the conductivity cell,  $T_{\text{cor}}$  is the lagged temperature of the seawater, and “ctcoeff” is a scaling coefficient that is a function of the profiling speed  $V_p$ . The profiling speed is defined as the velocity of the water at the CTD.

On shorter time scales, the approach used to correct for thermal inertia errors has traditionally relied on an idealized model developed by Lueck (1990) and slightly modified by Lueck and Picklo (1990) and Morison et al. (1994). The model, hereafter referred to as L&P90, is essentially a recursive filter that aims to estimate the short-term temperature anomaly of the volume of water present in the conductivity cell as the CTD travels through a seawater temperature gradient. It relies on two key parameters, namely,  $\alpha$  and  $\tau$ , that drive the amplitude and time scale of the filter. It is expressed in discrete form using the following equation (Morison et al. 1994):

$$T_{\text{short}}(n) = -bT_{\text{short}}(n-1) + a[T_{\text{cor}}(n) - T_{\text{cor}}(n-1)], \quad (4)$$

where  $T_{\text{short}}$  is the short-term temperature anomaly estimated by the filter, and  $n$  is the index for a discrete measurement. The two coefficients  $a$  and  $b$  are computed using

$$\begin{aligned} a &= \frac{4f_N \alpha \tau}{1 + 4f_N \tau}, \\ b &= 1 - \frac{2a}{\alpha}, \end{aligned} \quad (5)$$

where  $f_N$  is the Nyquist frequency, and  $\alpha$  and  $\tau$  are empirically determined parameters (see section 4).

The total estimated temperature of the sampled volume can be estimated by combining both of those temperature anomalies with the measured temperature:

$$T_{\text{cell}} = T_{\text{cor}} + T_{\text{anomaly}} = T_{\text{cor}} + T_{\text{long}} - T_{\text{short}}, \quad (6)$$

where  $T_{\text{cell}}$  is the estimated temperature of the sampled volume, corrected for both long- and short-term thermal inertia, and is used to derive the corrected salinity. The corrected salinity can then be derived from the measured conductivity and pressure, along the computed  $T_{\text{cell}}$ .

### 3. Datasets and methodology

#### a. Static accuracy and compressibility correction

The static accuracy of temperature and pressure were assessed utilizing data from four shipboard campaigns (Table A1), where RBR*concerto*<sup>3</sup> CTDs, which use equivalent thermistors and pressure sensors as the RBR*argo*<sup>3</sup>, were mounted on CTD rosettes equipped with SBE9 CTDs. The latter typically had two pairs of SBE4 temperature sensors and pressure was measured by a Paroscientific quartz sensor. The SBE9 is powered via a cable to the ship and reports back 24 Hz data. The accuracy of the SBE9 system post calibration is 0.001°C and 0.015% range for pressure (0.3 dbar). The RBR CTDs on the rosettes were internally recording and were typically set to sample at 8–12 Hz. A first gross comparison was made of the two SBE9 channels, and the primary was chosen for the temperature comparison below.

To compare pressure readings, the SBE9 and RBR data streams were interpolated to the RBR’s time base, and then the cross-correlations function was computed for pressure. The computed lags maximizing the cross-correlation function were then used to synchronize the data streams, exploiting the small (~1–2 dbar) pressure changes associated with surface wave action on the CTD fall and rise rates. Once synchronized, the difference of the pressures was found, and then binned every 20 dbar (using the SBE9 pressure) across all four voyages and all RBR CTDs (Table A1). In each 20 dbar bin, the distribution of pressure differences was calculated. A similar direct approach to examining temperature differences is precluded by the varying effect of water flow past the sensors within each rosette (the sensors are mounted at different heights above deck), and wake effects, which introduces both bias and noise to the comparison. To reduce these effects, we again use lagged correlations of the high-resolution temperature data streams from each sensor. For each cast and SBE9/RBR

sensor pair, we perform a lagged correction of temperature tendency in each 15 dbar bin. For bins where the temperature tendency correlation coefficient is  $>0.5$ , we apply the lag, typically between 0 and 1 s, to align the temperature traces and then find the temperature differences. Thus for bins where wake effects decorrelate the temperature variance, the data are not used. As for pressure, the temperature differences are binned to produce frequency distributions in 20 dbar pressure bins.

Laboratory measurements are preferable to in situ data for characterizing compressibility effects on the conductivity sensor. For example, the natural variability in the upper layer of the ocean is larger than the target accuracy of the conductivity sensor ( $\pm 0.003 \text{ mS cm}^{-1}$ ). In a laboratory pressure tank data are collected for a range of pressures up to the maximum pressure rating (i.e., 2000 dbar) of the RBRargo<sup>3</sup>. The temperature of the pressure tank is maintained between 1° and 2°C to represent ocean conditions at depth. The salinity in the pressure tank is determined from water samples before and after the pressure cycling using a Guildline 8400B Autosol and is used to remove the impact of the pressure tank on the conductivity measurements following the approach outlined in [appendix B](#).

The effects of compressibility on the conductivity measurement can be modeled using a cubic adjustment of the form

$$C_{\text{meas}} = \frac{C_{\text{raw}}}{1 + X2 \times P + X3 \times P^2 + X4 \times P^3}, \quad (7)$$

where  $C_{\text{raw}}$  is the raw conductivity measured by the instrument,  $P$  is the sea pressure,  $(X2, X3, X4)$  is the set of compressibility correction coefficients, and  $C_{\text{meas}}$  is the compressibility-corrected conductivity.

In situ data from two separate cruises (YMC in 2019 and RAPROCAN in 2022, see [Table A1](#)) were used to validate the compressibility correction determined at RBR's calibration laboratory for 12 separate CTDs. A direct comparison can thus be made between the compressibility-corrected salinity collected from the RBRargo<sup>3</sup> CTDs and the shipboard CTD, both cross calibrated with water samples (see [appendix B](#)).

### b. Sensor stability

A robust delayed-mode analysis method has been developed to identify salinity sensor drift in Argo profiling floats ([Owens and Wong 2009](#); [Cabanès et al. 2016](#)). [Nezlin et al. \(2020\)](#) used this method to characterize the long-term stability of the RBRargo<sup>3</sup> on six early-deployed Argo floats, to find that the salinity from the RBRargo<sup>3</sup> was stable through time over the duration of the available dataset. Here, we provide an update on the stability of the current RBRargo<sup>3</sup> fleet, using 19 RBRargo<sup>3</sup> floats that have been sampling in the ocean for over 6 months. The time series of salinity from these 19 RBRargo<sup>3</sup> CTDs are compared against objectively mapped salinity from a CTD reference database. Comparisons are done on isotherms selected from the least variable part of the  $T$ - $S$  curve in order to minimize the effects of natural variability in the comparison.

### c. Dynamic behavior of conductivity measurements

#### 1) RESPONSE TIME AND SENSOR MISALIGNMENTS

To align temperature and conductivity measurements collected by the RBRargo<sup>3</sup>, an optimal temporal lag is determined to correct the temperature observations. The optimal  $C$ - $T$  lag, which combines the two mechanisms detailed in [section 2](#), is determined by maximizing the cross correlation between the first-order differences in conductivity and in temperature ([Barth et al. 1996](#); [Ullman and Hebert 2014](#); [Dever et al. 2020](#)). This approach relies on the assumption that changes in conductivity over short spatial scales are mostly driven by changes in temperature. The analysis is applied to data collected by six different RBRargo<sup>3</sup> units deployed over different cruises (see [Table A1](#)). Only downcasts sampling deeper than the mixed layer depth are used, as the RBRargo<sup>3</sup> were pointing downward in all deployments. The resulting dataset comprises a total of 380 profiles. Each considered profile is separated into 7 s segments. For each segment, the cross covariance between the first-order differences in temperature and in conductivity is computed for a series of lags. The lag maximizing the cross covariance is recorded if the cross covariance is greater than 0.5. Otherwise, the segment is rejected from the analysis, as it likely violates the fundamental assumption of this method. Segments located above the mixed layer depth are also ignored, as they would skew the results toward a maximum cross covariance at a zero lag. A second-order polynomial is fit to the cross-covariance function using three consecutive points centered on the lag maximizing the cross covariance. The polynomial's maximum determines the "optimal lag" for the segment. Fitting a polynomial allows for noninteger lags, which is key to further remove dependence on the sampling rate. Finally, the optimal lags determined from all eligible segments are concatenated into a probability distribution function (PDF) as a function of the profiling speed averaged over the length of the segment. A total of 25 488 segments are considered to determine the  $C$ - $T$  lag for the thermistor on the RBRargo<sup>3</sup>. A Gaussian distribution is fit to the PDF in each profiling rate bin to extract the mean value of the  $C$ - $T$  lag to be used to align temperature and conductivity readings.

#### 2) THERMAL INERTIA ERRORS

An idealized experimental setup was designed in the laboratory to characterize how the RBRargo<sup>3</sup> conductivity cell responds to thermal gradients. An RBRargo<sup>3</sup> CTD was transferred from a cold bath ( $T \approx 6^\circ\text{C}$ ) into a large recirculating flume in thermal equilibrium with the room temperature ( $T \approx 19^\circ\text{C}$ ,  $S \approx 30$ ) to simulate a temperature step change in saltwater. The flume consists of a channel 50 cm wide  $\times$  50 cm high and about 8 m long. At the upstream end of the channel, a collimator is used to smooth out the turbulence in the flow entering the channel. At the downstream end of the channel, a propeller forces water through the recirculating loop at a constant speed, which can be adjusted by changing the rotational speed of the propeller. The water speed is monitored upstream of the RBRargo<sup>3</sup> CTD by a current meter (NorTek Vector) with its sample volume

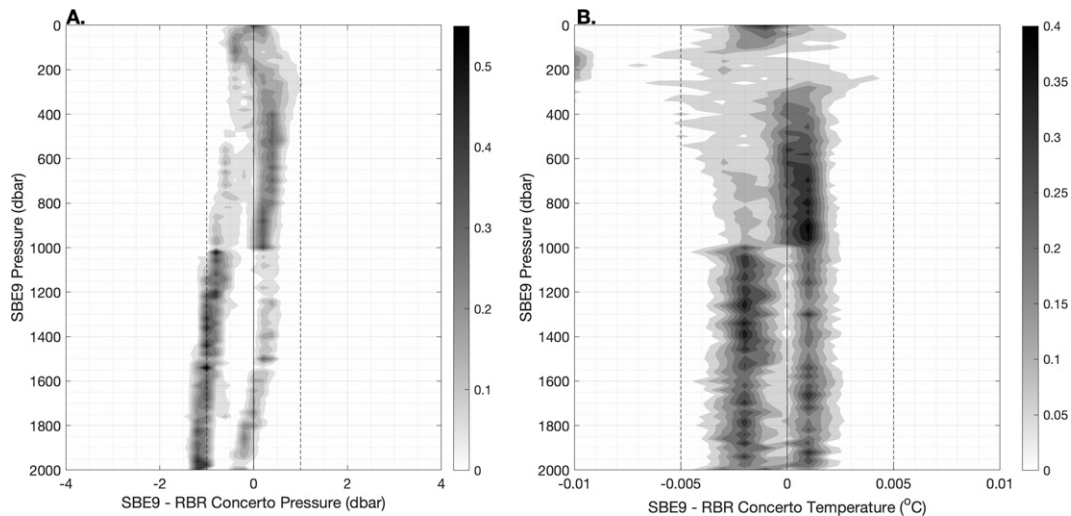


FIG. 3. (a) Pressure differences between SBE9 and the RBR $argo^3$ 's analogous RBR $concerto^3$ , across all voyages and sensor pairs, after synchronization (see section 3a). Plotted is the frequency distribution in each 20 dbar SBE9 pressure bin, expressed as a fraction of the total pairs in 0.2 dbar increments of the difference. (b) As in (a), but for temperature. Plotted is the frequency distribution in each 20 dbar SBE9 pressure bin, expressed as a fraction of the total pairs in 0.001°C increments of the difference.

centered on the same depth as the RBR $argo^3$  CTD. Six different water speeds were configured between 7 and 45  $\text{cm s}^{-1}$ , with two separate plunges at each speed.

A correction for the long-term adjustment of the conductivity cell is computed using Eq. (3). The coefficient  $ctcoeff$  is determined by doing a linear fit of the temperature anomaly as a function of the temperature difference between the interior of the conductivity cell and the water surrounding the cell. For each plunge, data collected in the first 90 s are ignored to avoid contamination from the short-term thermal inertia adjustment. The temperature anomaly is then binned to avoid overweighting the fit toward low temperature gradients across the conductivity cell.

The short-term error of the RBR $argo^3$  conductivity cell responds to thermal gradients with a time scale on the order of seconds, and cannot be addressed using the same approach as for its long-term counterpart, mostly for practical reasons. The physical processes driving this short-term adjustment are hypothesized to be related to the exchange of heat between the water located within the cell's channel, and the ceramic itself. It is operationally challenging to directly measure the temperature of the ceramic. L&P90 is used to correct the short-term thermal inertia on conductivity [see Eq. (4)]. The time scale of the short-term thermal inertia adjustment is estimated first, using a similar approach to Lueck and Picklo (1990): The slope of the logarithm of the normalized salinity time series is computed over the first 15 s after the temperature change to determine the  $e$ -folding time scale  $\tau$ , where  $t = 0$  is defined as the time where the marine temperature reaches 99% of its final value. The optimal value of  $\alpha$  is then computed by minimizing the root-mean-squared error (RMSE) in the salinity residuals referenced to the final static salinity.

A model linking the water speed and each coefficient required for dynamic corrections is obtained through a

linear regression analysis in log-space. The uncertainties on these regressions are computed from the standard deviation of the individual fits for each CTD tested in the flume. They are then propagated to the recommended values for an ascent rate of 10  $\text{cm s}^{-1}$  (nominal Argo float ascent rate) using a Monte Carlo method iterating 100 000 times.

The results obtained from the flume are validated using in situ datasets collected from two different profiling floats (see Table A2). These specific floats were selected for several reasons: First, it is important that the data resolution is high enough to capture the relevant time scales. In fact, most profiling floats transmit data that are binned into pressure bins, thus smoothing out the relevant time scales and making the thermal inertia corrections inefficient, especially over the shorter time scales. Second, it is necessary to have well-defined, sharp, interfaces followed by a well-mixed layer to be able to visualize the salinity adjustment due to thermal inertia. This is often the case in either thermohaline staircases, or at the base of the surface mixed layer. Finally, these floats were selected because they span different ocean basins (Caribbean Sea and subarctic North Atlantic), and a range of profiling speeds ranging from 3 to 20  $\text{cm s}^{-1}$ .

## 4. Results

### a. Static accuracy and compressibility correction

#### 1) PRESSURE AND TEMPERATURE ACCURACY

Figure 3 demonstrates the static accuracy of both pressure and temperature on the RBR $argo^3$  when compared to a SBE9 on a CTD rosette. The full dataset reveals that the instruments agree to within 1.5 dbar across all pressure ranges. For temperature, we find that the vast majority of paired readings give temperature differences less than 0.003°C, which is within the specifications of the SBE9 and RBR $argo^3$  CTDs, confirming

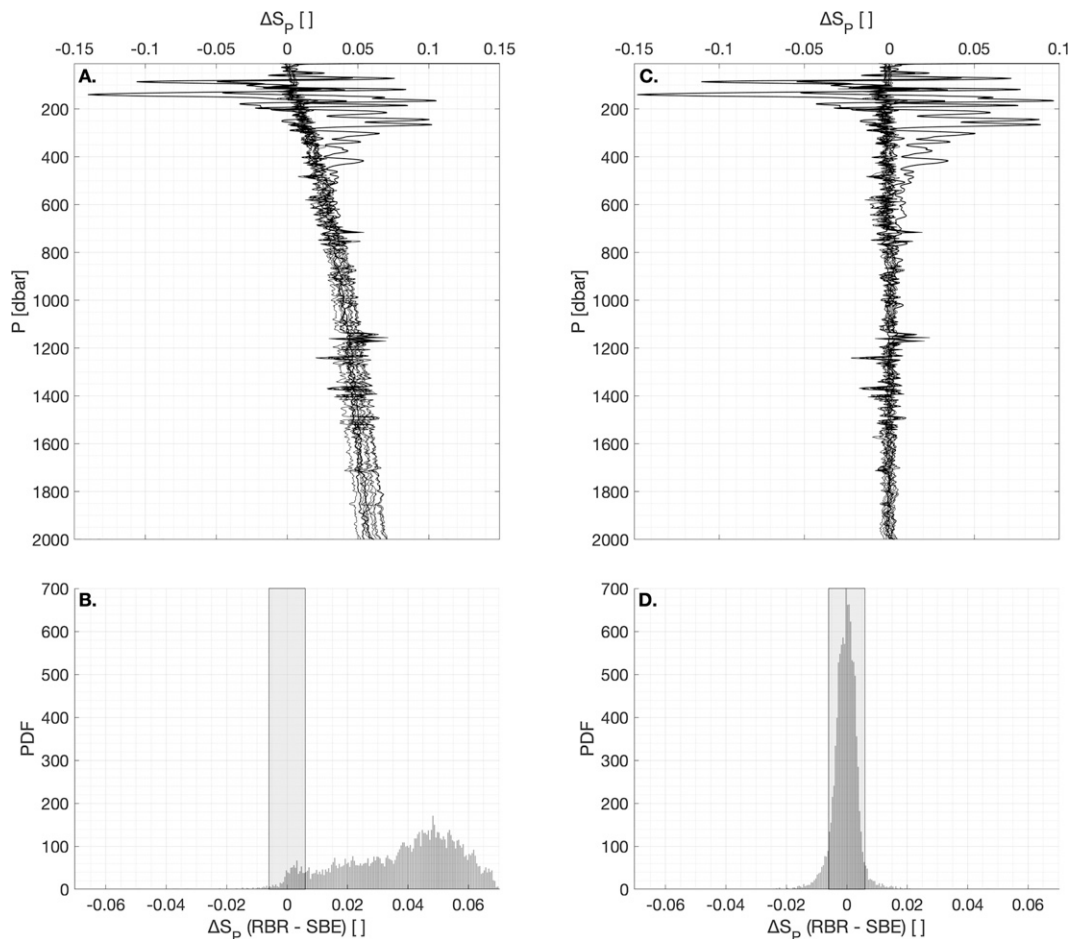


FIG. 4. Difference in salinity measurements between the RBR $argo^3$  and the shipboard SBE9 during the YMC (station 4; Rees and McMahon 2019) and RAPROCAN (station 45) cruises (see appendix B). (a) Before and (c) after applying a customized pressure correction to conductivity. (b),(d) The corresponding probability distribution functions (PDFs) of the salinity bias for data collected below 800 m. All CTDs were cross calibrated using bottle samples taken on this profile (see section 2 and appendix B).

the stated accuracy for temperature on the RBR $argo^3$  across the pressure ranges examined.

## 2) CONDUCTIVITY STATIC ACCURACY

The amplitude of the compressibility error was characterized by directly comparing the salinity profiles obtained from an SBE9 and RBR $argo^3$  CTDs on a variety of cruises. Comparing the two salinity records in the deeper part of the water column (e.g., >800 dbar), where the water masses tend to be more stable, revealed that the salinity difference between the RBR $argo^3$  CTDs and the shipboard cross-calibrated SBE9 has a depth-dependent bias. An example of this bias is shown in Fig. 4. RBR $argo^3$  CTDs have a salty bias that increases with depth, suggesting that the error in salinity is caused by the compressibility of the conductivity cell.

All 12 RBR $argo^3$  CTDs deployed during the YMC and RAPROCAN cruises were tested for pressure response in the laboratory, using the setup described in section 3.

Customized coefficients were derived for each RBR $argo^3$  CTD, reducing the compressibility-induced salinity error from  $O(0.05)$  to  $O(0.003)$  (Fig. 5). The field-based comparison confirms the validity of the newly derived compressibility correction coefficients from the laboratory: after updating the coefficients in Eq. (7), all 12 RBR $argo^3$  CTD compare well to the calibrated SBE9 data, with residuals contained within the combined accuracies of the RBR $argo^3$  and the SBE9 CTDs (Fig. 4). Not only is the mean of the PDF brought closer to 0, but its standard deviation is also reduced, suggesting that the salinity bias is less dependent on depth. These results indicate that customized parameters for compressibility correction to conductivity can reliably be determined for individual RBR $argo^3$  CTDs in the laboratory during the calibration process.

### b. Sensor stability

Since the average length of the time series from the 19 considered RBR $argo^3$  CTDs was only 1.5 years, it is somewhat

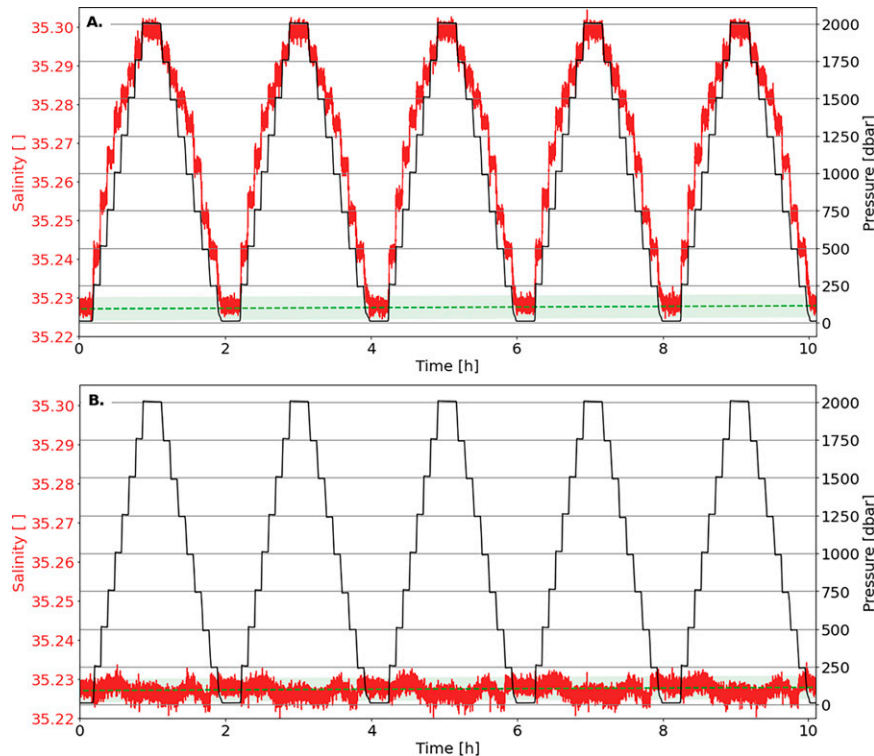


FIG. 5. Time series of practical salinity (red line) during pressure cycling (black line). (a) Before pressure correction is applied and (b) after the cubic pressure correction has been applied for the RBRargo<sup>3</sup> CTD SN060671. The reference salinity is superimposed (dashed green line), with its associated uncertainties (green shading).

premature to draw any definite conclusions about the long-term stability of the RBRargo<sup>3</sup> CTDs. Nonetheless, salinity measurements from 18 RBRargo<sup>3</sup> CTDs showed no sign of sensor drift at the time of analysis, suggesting good sensor stability (Fig. 6). Only one RBRargo<sup>3</sup> suffered from significant drifting (WMO5906299), which was identified to be associated with a malfunction of the float's buoyancy pump. The float was found to have extended surfacing times, sometimes over 24 h, that correlated with sudden and large

fresh salinity errors, suggesting the cell suffered from biofouling due to the abnormally long surfacing time (RBR 2021). For the remaining 18 RBRargo<sup>3</sup> CTDs, totaling 857 profiles to date, 94% of profiles have a salinity anomaly smaller than  $\pm 0.01$ , falling within Argo's expectation. As in section 2, an offset from reference was present for most of the analyzed CTDs, which is due to the suboptimal compressibility coefficients used on these RBRargo<sup>3</sup> CTDs, as previously discussed.

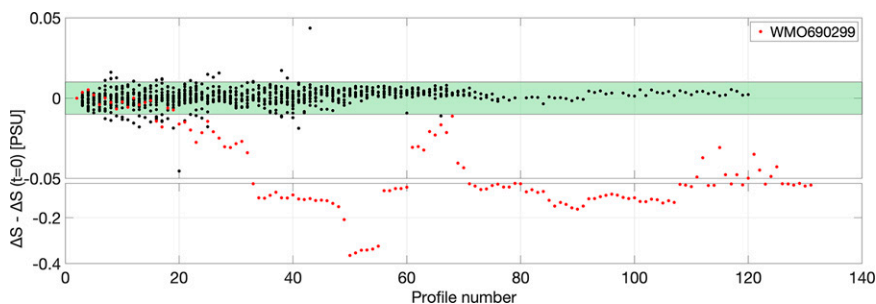


FIG. 6. Time series of the salinity bias determined from objectively mapped reference data (Owens and Wong 2009) with respect to the first full-depth profile, for 19 RBRargo<sup>3</sup> CTDs. The green shading indicates  $\pm 0.01$ . Float with WMO5906299 is highlighted in red, as it was identified to drift due to a float malfunction (see section 4). Note the break and change in scale in the y axis.

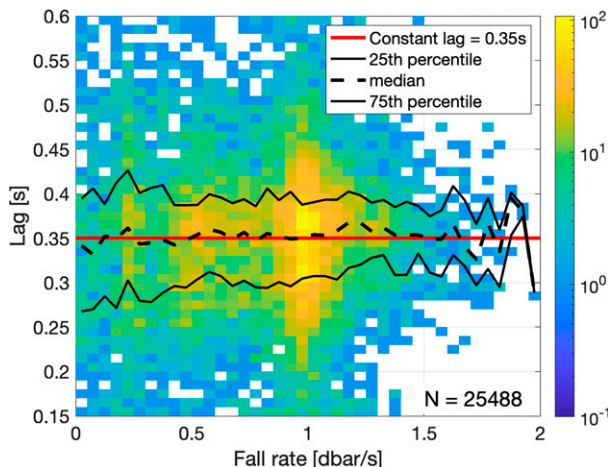


FIG. 7. Two-dimensional PDF of the “optimal”  $C-T$  lag derived for 25 488 segments, as a function of fall rate (see section 3). Note the logarithmic color scale.

c. Dynamic behavior of conductivity measurements

1) RESPONSE TIME AND SENSOR MISALIGNMENTS

The misalignment between temperature and conductivity measurements (i.e.,  $C-T$  lag) introduced by the slower time response of the thermistor is characterized by applying the analysis detailed in section 3. The distribution of “optimal”  $C-T$  lags derived from the dataset is shown in Fig. 7.

Several key points can be extracted from Fig. 7: First, the spread between the 25th and 75th percentiles with respect to the median value is comparable across fall rates, suggesting that the distribution of optimal lags can be approximated by a normal distribution. Second, the median value computed for each individual fall-rate bin is fairly constant and thus does not seem to be a function of the fall rate, over the range of rates explored. Third, a constant optimal lag of 0.350 s ( $\sigma = 0.003$  s) can be used for fall rates slower than  $1.5 \text{ dbar s}^{-1}$ .

To validate this empirically derived  $C-T$  lag with an independent dataset, an RBRargo<sup>3</sup> CTD is used in the laboratory to profile downward through a sharp temperature gradient (Fig. 8; Schmitt et al. 2005). It is clear in Fig. 8 that the time response of the temperature lags the response of the conductivity measurements: Not only the interface is smoother in the temperature signal than it is in the conductivity measurements, but it is also shifted in time (and thus pressure). The computed salinity exhibits a spike just after the RBRargo<sup>3</sup> CTD crossed the interface, with a maximum error of 1.5. Once the  $C-T$  lag correction is applied, the interfaces in both temperature and conductivity are centered around  $\sim 3$  dbar. Spiking observed in the raw salinity is now much reduced and the bottom layer is more homogeneous.

2) THERMAL INERTIA ERRORS

Figure 9 presents the results from one of the plunges made in the saltwater flume. It shows the two dominant

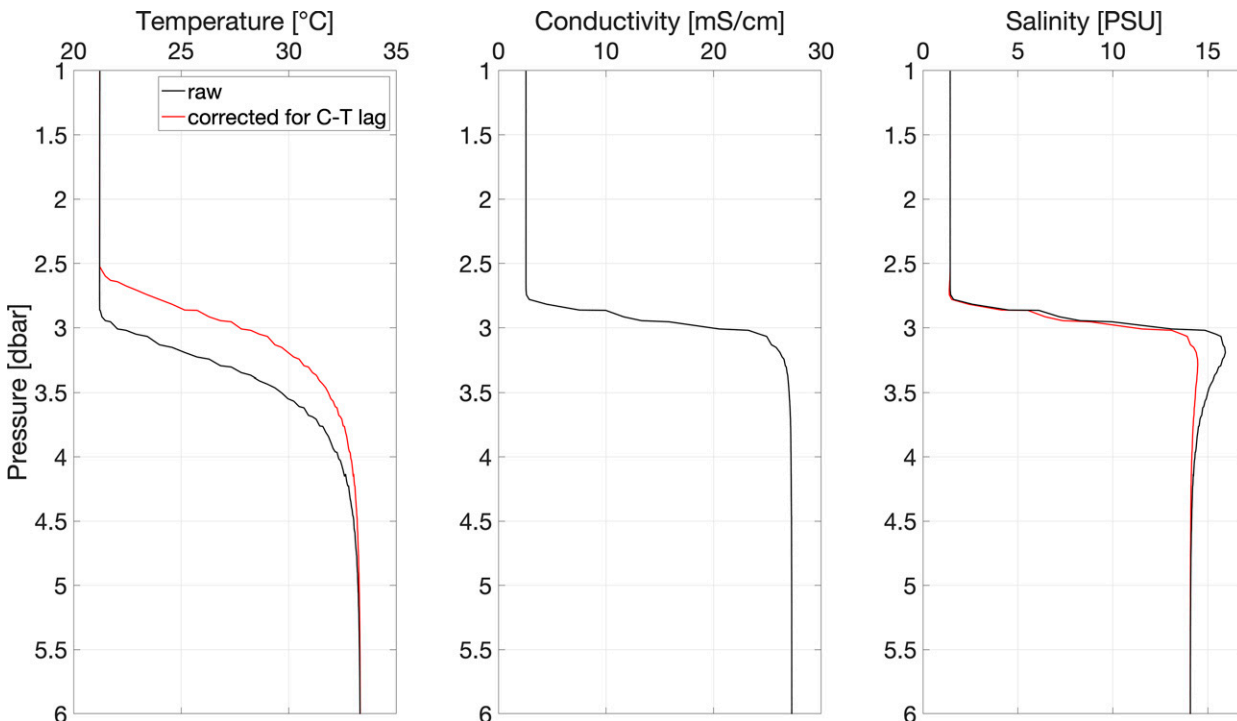


FIG. 8. Profiles of temperature, conductivity, and salinity obtained using an RBRargo<sup>3</sup> profiling through a sharp temperature and conductivity interface in a tall water tank (Schmitt et al. 2005). Black lines represent the raw data, while the red lines show the data after lagging the temperature by  $-0.35$  s. Salinity spiking appears to be reduced after lagging the temperature signal.

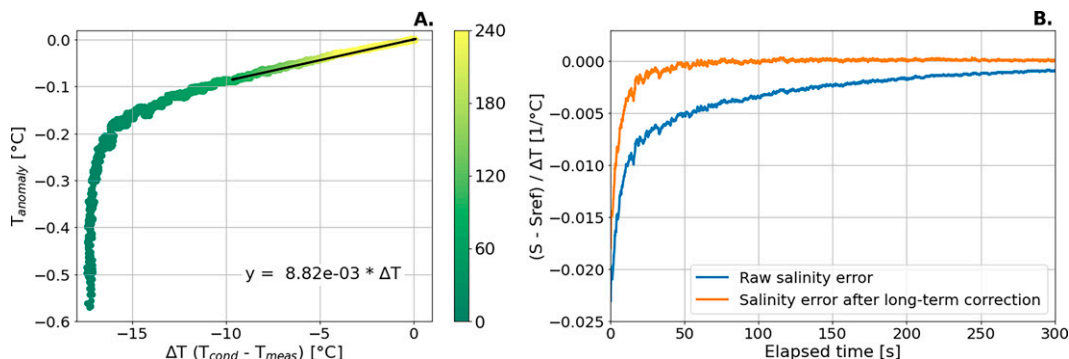


FIG. 9. Example of long-term correction for SN208077 from a single plunge in the saltwater flume at a flow speed of  $13.2 \text{ cm s}^{-1}$ . (a) Computed temperature anomaly  $T_{\text{anomaly}}$  as a function of the temperature difference between  $T_{\text{cond}}$  and  $T_{\text{meas}}$  (see section 3). Color map shows the time elapsed since the temperature step change (in s), and the solid black line shows the least squares fit used to compute  $\text{ctcoeff}$ . (b) Time series of salinity error during the plunging test, normalized to the temperature gradient (see section 2). Raw salinity (blue) is shown along with the corrected salinity (orange) using Eq. (3) and  $\text{ctcoeff} = 8.82 \times 10^{-3}$ .

time scales of the thermal inertia adjustment of the salinity after experiencing a temperature change, and highlights the change in physical processes responsible for those two different time scales. At first, the salinity error normalized by the temperature change, is as large as  $0.02 \text{ }^\circ\text{C}^{-1}$  and rapidly adjusts with a characteristic time scale on the order of tens of seconds. During this first phase, the temperature difference between the water and the internal cell temperature does not constitute a good predictor, suggesting that the driving mechanism is the heat exchange between the ceramic and the sampled water volume, as hypothesized in section 3. For longer time scales ( $>30 \text{ s}$ ), the temperature gradient across the conductivity cell  $\Delta T$  becomes a good predictor of the thermal inertia temperature anomaly. As  $\Delta T$  decreases and the conductivity cell reaches thermal equilibrium with its surrounding water, the corresponding temperature anomaly decreases linearly with a constant slope. Once the long-term correction is applied using Eq. (3), the transient salinity error depicted in Fig. 9 is greatly reduced. The remaining thermal inertia error is now mostly constrained to the first tens of seconds after the temperature step. For example, at  $V_p = 13.2 \text{ cm s}^{-1}$ , the salinity error after 60 s drops from  $5 \times 10^{-3}$  to  $5 \times 10^{-4} \text{ }^\circ\text{C}^{-1}$ .

The remaining error in the salinity is attributed to the thermal inertia adjustment over short time scales. This adjustment over shorter time scales can be seen in the time series of the normalized salinity in Fig. 10, where the logarithm of the normalized salinity decreases linearly with time. A linear fit over the first 15 s after the temperature step yields an estimate of the  $e$ -folding time scale  $\tau$ . For example, at  $V_p = 13.2 \text{ cm s}^{-1}$ , the normalized salinity decreases with a time constant of  $\tau = 7.5 \text{ s}$ . Using this decaying time scale, it is found that  $\alpha = 0.03$  minimizes the RMSE of the salinity residuals. Figure 10 shows the time series of salinity residuals after correcting for both the long- and short-term thermal inertia errors for  $V_p = 13.2 \text{ cm s}^{-1}$ , with a maximum salinity residual on the order of  $1 \times 10^{-4} \text{ }^\circ\text{C}^{-1}$ .

All three coefficients used in correcting for thermal inertia errors are expected to vary with the profiling speed  $V_p$ , as the profiling speed affects the thickness of the boundary layer around the conductivity cell, in turn changing the magnitude and time scale of the heat fluxes (Lueck 1990; Morison et al. 1994). Figure 11 shows how each of the coefficients varies with the flow speed. All three coefficients can be fit to a power law:

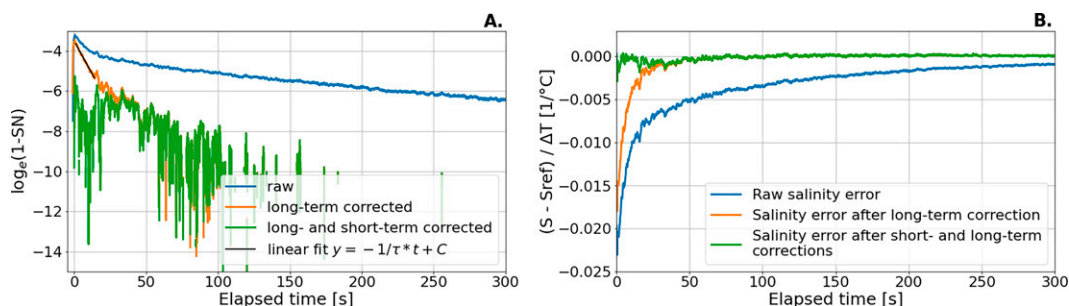


FIG. 10. Example of short-term correction for SN208077 at a flow speed of  $13.2 \text{ cm s}^{-1}$ . (a) Time series of the normalized salinity error. The linear fit used to derive the time scale  $\tau$  [see section 2 and Eq. (5)] is shown as the solid black line. (b) Time series of the salinity error during the plunging test normalized to the temperature gradient, similarly to Fig. 9.

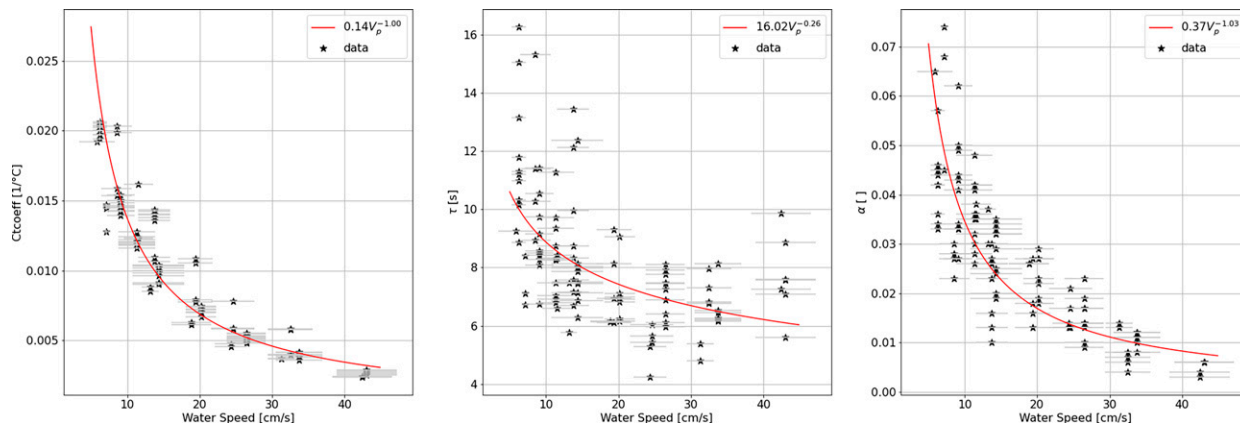


FIG. 11. Values of the measured  $ctcoeff$ ,  $\tau$ , and  $\alpha$  as a function of the flume speed  $V_p$  (black stars). The standard deviation in the water speed measured during each plunge is shown as error bars. A power-law least squares fit is applied to the data (red line).

$$ctcoeff = (0.14 \pm 0.02) \times V_p^{-1.00 \pm 0.04}$$

$$\alpha = (0.37 \pm 0.11) \times V_p^{-1.03 \pm 0.19}$$

$$\tau = (16.02 \pm 4.55) \times V_p^{-0.26 \pm 0.09}$$

which, for the nominal speed of Argo floats of  $10 \text{ cm s}^{-1}$ , yields  $ctcoeff = 0.014(\pm 0.002)$ ,  $\alpha = 0.035(\pm 0.021)$ , and  $\tau = 8.80(\pm 3.2) \text{ s}$ .

The validity of the thermal inertia correction across a range of profiling speeds is assessed using an Argo float profiling in the subarctic North Atlantic. The float was set to profile at different speeds, ranging from 3 to  $20 \text{ cm s}^{-1}$ . Figure 12 shows the effect of the dynamic correction algorithm at four different speeds. While the amplitude of the correction is relatively small, due to the small temperature gradient, the corrected salinity does demonstrate reduced spiking at the interface (particularly visible at higher speeds), and a more homogeneous mixed layer over both shorter and longer time scales.

## 5. Discussion

The accuracy of both temperature and pressure on the RBRargo<sup>3</sup> CTD is proven to be within the expected accuracy of the Argo program ( $\pm 0.002^\circ\text{C}$  and  $\pm 2.4 \text{ dbar}$ , respectively; Wong et al. 2020), throughout the range of typical pressure experienced by a Core Argo float (i.e., 2000 dbar).

While salinity is calibrated at the factory to be within the Argo accuracy requirements at atmospheric pressure ( $\pm 0.01$ ), a salinity error is introduced as pressure increases due to the physical deformation of the conductivity cell. This salinity bias is known to affect both inductive and electrode-based CTDs: while a salty bias is observed at depth in the RBRargo<sup>3</sup>, the electrode-based SBE41CP reports a fresh bias at depth (Sea-Bird 2013). A unit-based compressibility correction to conductivity is determined using a laboratory setup where each RBRargo<sup>3</sup> is pressurized in saltwater and a cubic correction to conductivity is derived (Fig. 5). The proposed correction is validated in the field and is proven to reduce the salinity bias with pressure (Fig. 4).

Of the 19 RBRargo<sup>3</sup> CTDs deployed for longer than 6 months, only one was found to drift, which has been linked to a float malfunction leading to an excessive surface time likely enabling significant biofouling to occur (Fig. 6; RBR 2021). Despite the relatively short time series available (average of 1.5 years), the RBRargo<sup>3</sup> CTD presents an encouraging long-term salinity stability with 94% (99.8%) of profiles within  $\pm 0.01$  (0.02) of the reference dataset.

For a profiling platform such as Argo floats, dynamic errors can significantly affect the quality of the data. A robust statistical analysis based on existing literature (Barth et al. 1996; Dever et al. 2020) determines that an optimal  $C-T$  lag of 0.35 s helps minimize salinity spiking for the RBRargo<sup>3</sup> CTD. The absence of fall-rate dependence on the  $C-T$  lag demonstrates that the thermistor and conductivity cell are relatively well aligned in space, thus minimizing the advective component of the  $C-T$  lag (Fig. 7). The value determined here compares well with the previous estimate obtained in Halverson et al. (2020a) using a different method. Some minimal spiking would remain, however, due to the fact that the temperature signal would be smoother than the conductivity readings, as it is clearly observed in Fig. 8. This remaining error can be mitigated by smoothing the conductivity signal, or by applying a sharpening algorithm to the temperature, as suggested in Halverson et al. (2020a). Inferring an unresolved high-frequency signal is a highly subjective task and is thus left to the discretion of the data user. The uncertainty in the optimal  $C-T$  lag obtained from the distribution in Fig. 7 inevitably leads to an uncertainty in the corrected salinity. The magnitude of the propagated error is directly proportional to the temperature gradient and the ascent rate. As an example, a temperature gradient of  $1^\circ\text{C m}^{-1}$  sampled at an ascent rate of  $10 \text{ cm s}^{-1}$  leads to a gradient of  $0.1^\circ\text{C s}^{-1}$ . The standard deviation in the determined optimal  $C-T$  lag ( $\sigma = 0.003 \text{ s}$ ) thus generates an error of about  $3 \times 10^{-4}^\circ\text{C}$ , leading to an error in salinity of approximately  $3 \times 10^{-4}$ .

Thermal inertia errors affecting salinity from the RBRargo<sup>3</sup> CTD exhibit two separate time scales. The long-term thermal inertia error has a time scale  $O(120) \text{ s}$ , and generates an error

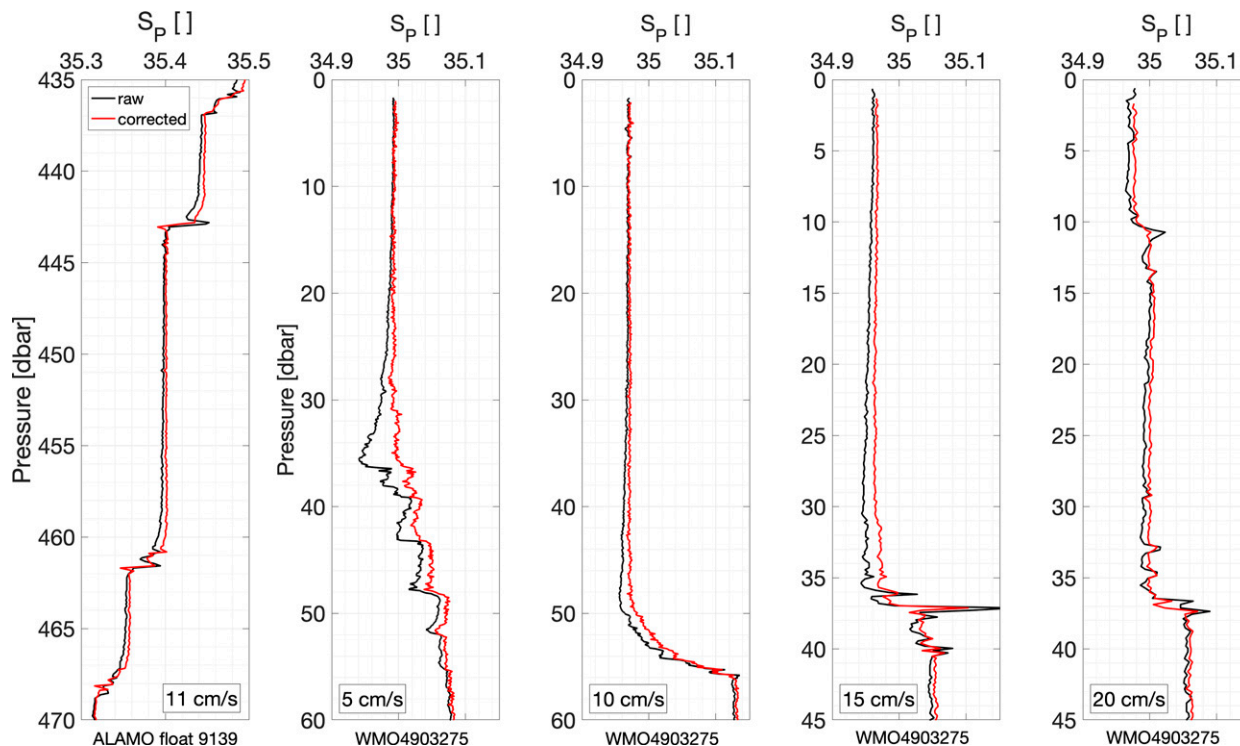


FIG. 12. Profile of practical salinity collected by floats 9139 (see Fig. 2) and WMO4903275 at 1 Hz and at different profiling speeds as the float crosses a  $1.5^{\circ}\text{--}2^{\circ}\text{C}$  temperature change. Raw data are shown in black, while data corrected for dynamic errors are shown in red.

on salinity about 4 times smaller than its short-term counterpart (Fig. 13). The correction for this second-order thermal inertia error is based on the direct measurement of the instantaneous temperature difference between the inside of the conductivity cell and the marine temperature. Implementing the correction as a function of the temperature difference presents key advantages: First, it does not require an explicit time scale, as the time scale is implicitly included in the

temperature gradient. Second, it prevents the propagation of spurious measurement anomalies throughout the time series, as a recursive filter like L&P90 would. And third, being an instantaneous correction, it has significant operational advantages as implementing the correction on board autonomous platforms such as Argo floats is greatly simplified. Just like the  $C\text{--}T$  lag, the uncertainty associated with the parameter  $\text{ctcoeff}$  that propagates onto the computed salinity can be

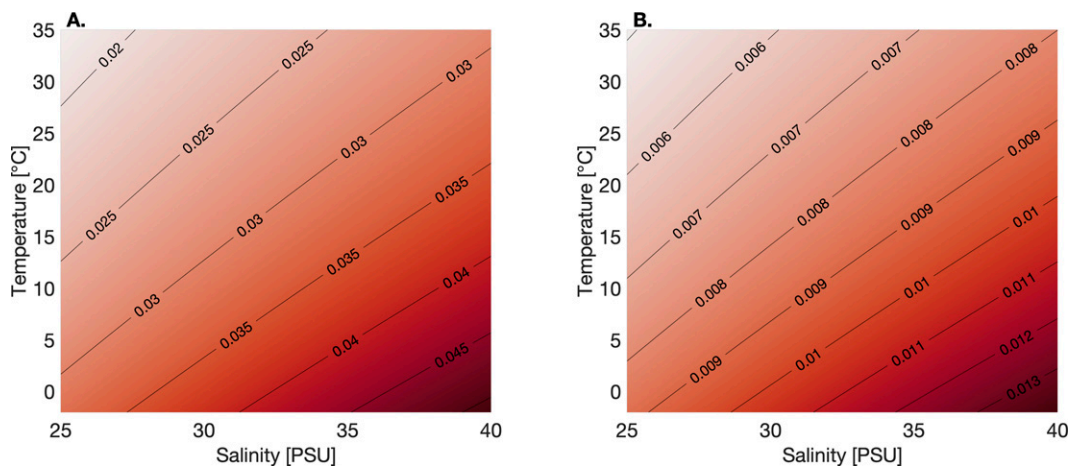


FIG. 13. Amplitude of the salinity error (in  $^{\circ}\text{C}^{-1}$ ) corrected by (a) the short-term and (b) the long-term thermal inertia corrections, as a function of the measured temperature and salinity.

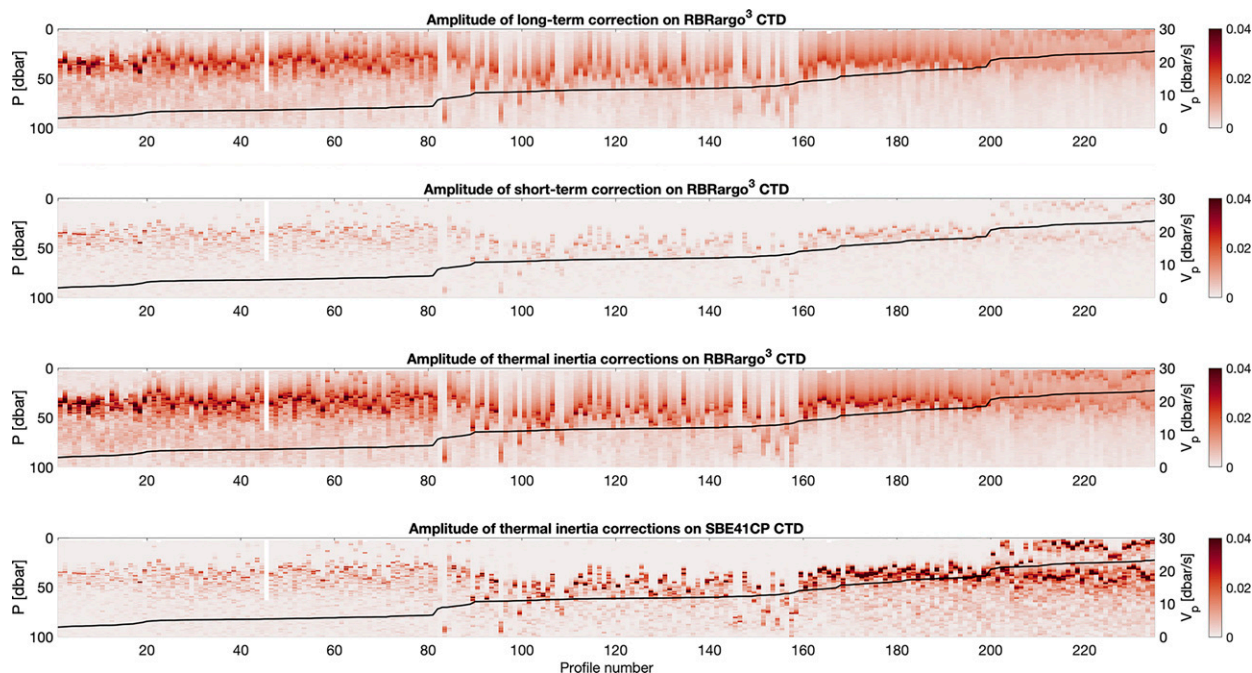


FIG. 14. Amplitude of the salinity correction for thermal inertia determined from high-resolution profiles collected by WMO4903275 at the base of the mixed layer. Row show (from top to bottom) long-term correction on an RBRargo<sup>3</sup>, short-term correction on an RBRargo<sup>3</sup>, total thermal inertia correction on an RBRargo<sup>3</sup>, and total thermal inertia correction for a SBE41CP (Johnson et al. 2007). Profiles are organized by increasing profiling speed  $V_p$ .

estimated by considering once more a temperature gradient of  $0.1^\circ\text{C s}^{-1}$  sampled at  $10\text{ cm s}^{-1}$ . The propagated uncertainty on the salinity correction from the long-term thermal inertia correction is  $<1 \times 10^{-3}$ .

A short-term error is observed on a time scale of 5–10 s, and is corrected for using the L&P90 recursive model. As suggested in Morison et al. (1994), the correction is applied by inferring the temperature of the sampled volume based on the marine temperature history [see Eq. (4)]. The amplitude of the correction on the salinity is thus both temperature and salinity dependent, and is dictated by the  $a$  parameter in Eq. (5) (see Fig. 13). The uncertainty of the correction using the L&P90 model is difficult to estimate, as it first requires estimating a time scale of the adjustment (i.e.,  $\tau$ ), and a corresponding amplitude ( $\alpha$ ). Additionally, these two parameters have been observed to be interdependent (Morison et al. 1994; Lueck and Picklo 1990; Martini et al. 2019), suggesting that the uncertainty associated with the inferred time scale also affects the amplitude of the correction. Finally, the L&P90 model being a recursive filter, the error in the correction associated with the model's parameters uncertainty accumulates through time.

For comparison, the amplitude of the short-term thermal inertia correction on the RBRargo<sup>3</sup> is about 3 times smaller than the corrections currently applied to CTD data collected from an SBE41CP, and operates over similar time scales (Johnson et al. 2007). While the long-term thermal inertia correction on the RBRargo<sup>3</sup> has a comparable amplitude to the short-term correction, its longer time scales implies

that the error is smeared over a larger part of the profiles. In particular, profiles collected in tropical waters would be more affected by thermal inertia errors due to the temperature gradients in these regions, often characterized by deeper and sharper temperature gradients. The total amplitude of thermal inertia corrections on the RBRargo<sup>3</sup> is highly dependent on the vertical temperature structure of the water column and is therefore difficult to characterize theoretically. An example of the amplitude of each thermal inertia correction is shown in Fig. 14 using the high-resolution data returned by the float for a short period of time (see Table A2). As expected, the maximum amplitude of the thermal inertia correction on a RBRargo<sup>3</sup> is weaker than on the SBE41CP, but the correction affects a larger portion of the water column, due to the long-term component of the thermal inertia.

Because thermal inertia errors are generated from the heat exchange between the conductivity cell and its surrounding water, the thermal inertia corrections derived in this study are expected to be a function of the profiling speed. The range of speeds explored in the flume not only encompasses the nominal speed for Argo floats ( $\sim 10\text{ cm s}^{-1}$ ), but also covers the realistic range of speeds an autonomous profiling platform can achieve (e.g., floats, gliders). The relationships linking the three coefficients to profiling speed are modeled using a power law, as the theoretical work from Lueck (1990) suggests, but it is not intended to be anything more than an empirical fit. Caution should be used when extrapolating coefficients outside of the range of explored

TABLE A1. List of the datasets obtained from field cruises used to characterize the RBRargo<sup>3</sup>. Institution abbreviations are as follows: DFO: Department of Fisheries and Ocean; JAMSTEC: Japan Agency for Marine-Earth Science and Technology; WHOI: Woods Hole Oceanographic Institution; CSIRO: Commonwealth Scientific and Industrial Research Organisation; IEO Instituto Español de Oceanografía.

Cruise name	Partner institution	Year	Ocean basin	RBRargo <sup>3</sup> SNs
Line P	DFO Canada	2018	Northeast Pacific Ocean	060672
JAMSTEC	JAMSTEC	2018	Northwest Pacific Ocean	060669, 060671
PEACH	WHOI	2018	Northwestern Atlantic Ocean	060667, 060668, 060671
AR41	WHOI	2019	Northwestern Atlantic Ocean	060667, 060668, 060670
YMC	CSIRO/WHOI	2019	Southeastern Indian Ocean	060669, 060671
RAPROCAN	IEO	2022	Eastern tropical Atlantic Ocean	209887 to 209996

speeds, such as for typical CTD rosette profiling speeds (e.g., 100 cm s<sup>-1</sup>).

One of the most important results is maybe the power-law dependence of the thermal inertia corrections on the flow rate (Fig. 11). The main consequence is that the thermal inertia correction is thus less sensitive to uncertainties in both coefficients and flow rates when profiling at higher speeds. To minimize the uncertainty on the thermal inertia correction, it is therefore recommended to profile at higher speeds, which could be compensated with a higher sampling rate to preserve vertical resolution. This can be directly observed in Figs. 12 and 14, where the salinity error visible in the raw in situ data is clearly smaller at faster speeds, despite crossing a similar temperature gradient (1.5°–2°C).

For an RBRargo<sup>3</sup> profiling at approximately 10 cm s<sup>-1</sup> the best practices for dynamic correction can be summarized as 1) lagging the temperature signal by –0.35 s, 2) correcting for the long-term thermal inertia error using Eq. (3) and  $c_{\text{coeff}} = 1.4 \times 10^{-2}$ , and 3) correcting for the short-term thermal inertia error using L&P90 [Eqs. (4) and (5)] with  $\alpha = 0.035$  and  $\tau = 8.80$  s.

*Acknowledgments.* Drs. Owens and Richards contributed to the characterization of the thermal inertia errors. Dr. Wijffels led the validation of pressure and temperature measurements on a RBRargo<sup>3</sup>. Dr. Wong conducted the analysis of salinity measurement stability. Drs. Shkvorets, Halverson, and Johnson provided support in the experimental design and analysis of the compressibility error in salinity. Thanks go to the Argo community at large, for their support in facilitating deployments of RBRargo<sup>3</sup> CTDs, in providing ancillary datasets, and in offering feedback on the analysis. Special thanks are directed to the “Argo RBR Data Task Team,” specially formed to collaborate on the analysis of the RBRargo<sup>3</sup>.

*Data availability statement.* The data used in this work are available in a dedicated GitHub repository: [https://github.com/matdever/RBRargo3\\_paper](https://github.com/matdever/RBRargo3_paper).

The code necessary to produce the displayed figures is also included in the repository.

## APPENDIX A

### Datasets

This appendix lists the datasets used to characterize the RBRargo<sup>3</sup>. Table A1 describes the datasets obtained from field cruises, while Table A2 gives details of the datasets obtained from profiling floats.

## APPENDIX B

### Calibration of Rosette Data

Similar to SBE911 cross-calibration protocol, bottle salinity samples collected from the CTD rosette can be used to cross calibrate RBRargo<sup>3</sup> CTDs mounted on a shipboard rosette. Inductive conductivity cells, like the one on the RBRargo<sup>3</sup>, are subject to the proximity effect: any material located within a 15 cm radius from the conductivity cell would affect measurements of conductivity in a multiplicative way (Halverson et al. 2020b). The multiplicative factor is named the  $K$  factor:

$$C = K \times C_{\text{raw}}. \quad (\text{B1})$$

A conductive material, such as a metal, would generate a  $K$  factor smaller than 1 (i.e., the apparent conductivity would appear larger than the one of the water), while an insulating material such as plastic would lead to a  $K$  factor greater than 1 (i.e., the apparent conductivity would appear smaller than the one of the water). The two RBRargo<sup>3</sup> CTDs mounted on the rosette during the YMC cruise on board the R/V *Investigator* in 2019 (Rees and McMahon 2019), as well as the 10 RBRargo<sup>3</sup> CTDs deployed as part of the RAPROCAN cruise are cross calibrated with salinity water samples measured using an Autosal Guildline using a zero-intercept linear fit [see Eq. (B1)].

TABLE A2. List of the datasets obtained from profiling floats used to characterize the RBRargo<sup>3</sup>.

Float type	Float ID	Data resolution	Institution	Year	Ocean basin
ALAMO	9139	1 Hz	WHOI	2017	Caribbean Sea
Argo float	WMO4903275	0.10 dbar bins	WHOI	2020	North Atlantic

## REFERENCES

- Barth, J. A., R. O'Malley, J. Fleischbein, R. L. Smith, and A. Huyer, 1996: SeaSoar and CTD observations during the coastal jet separation cruise W9408A, August to September 1994. CJS Tech. Rep. 162, 170 pp.
- Bittig, H. C., B. Fiedler, R. Scholz, G. Krahnemann, and A. Körtzinger, 2014: Time response of oxygen optodes on profiling platforms and its dependence on flow speed and temperature. *Limnol. Oceanogr. Methods*, **12**, 617–636, <https://doi.org/10.4319/lom.2014.12.617>.
- Cabanes, C., V. Thierry, and C. Lagadec, 2016: Improvement of bias detection in Argo float conductivity sensors and its application in the North Atlantic. *Deep-Sea Res. I*, **114**, 128–136, <https://doi.org/10.1016/j.dsr.2016.05.007>.
- Dever, M., M. Freilich, J. T. Farrar, B. Hodges, T. Lanagan, A. J. Baron, and A. Mahadevan, 2020: EcoCTD for profiling oceanic physical–biological properties from an underway ship. *J. Atmos. Oceanic Technol.*, **37**, 825–840, <https://doi.org/10.1175/JTECH-D-19-0145.1>.
- Fofonoff, N. P., S. P. Hayes, and R. C. Millard, 1974: WHOI/Brown CTD microprofiler: Methods of calibration and data handling. Woods Hole Oceanographic Institution Tech. Rep., 67 pp., <https://doi.org/10.1575/1912/647>.
- Fozdar, F. M., G. J. Parkar, and J. Imberger, 1985: Matching temperature and conductivity sensor response characteristics. *J. Phys. Oceanogr.*, **15**, 1557–1569, [https://doi.org/10.1175/1520-0485\(1985\)015<1557:MTACSR>2.0.CO;2](https://doi.org/10.1175/1520-0485(1985)015<1557:MTACSR>2.0.CO;2).
- Halverson, M., I. Shkvoret, and G. Johnson, 2020a: Dynamic corrections for the RBR Argo CTD 2000dbar. RBR Tech. Rep., 26 pp., <https://oem.rbr-global.com/floats/files/5898249/34668603/1/586804683000/0008228revA+Dynamic+corrections+for+the+RBRargo+CTD+2000dbar.pdf>.
- , E. Siegel, and G. Johnson, 2020b: Inductive-conductivity cell: A primer on high accuracy CTD technology. *Sea Technology*, Vol. 61, No. 2, 24–27.
- Horne, E. P. W., and J. M. Toole, 1980: Sensor response mismatches and lag correction techniques for temperature-salinity profilers. *J. Phys. Oceanogr.*, **10**, 1122–1130, [https://doi.org/10.1175/1520-0485\(1980\)010<1122:SRMALC>2.0.CO;2](https://doi.org/10.1175/1520-0485(1980)010<1122:SRMALC>2.0.CO;2).
- Jayne, S. R., and N. M. Bogue, 2017: Air-deployable profiling floats. *Oceanography*, **30** (2), 29–31, <https://doi.org/10.5670/oceanog.2017.214>.
- Johnson, G. C., 2020: Comments on “Corrections for pumped SBE 41CP CTDs determined from stratified tank experiments.” *J. Atmos. Oceanic Technol.*, **37**, 351–355, <https://doi.org/10.1175/JTECH-D-19-0098.1>.
- , J. M. Toole, and N. G. Larson, 2007: Sensor corrections for Sea-Bird SBE-41CP and SBE-41 CTDs. *J. Atmos. Oceanic Technol.*, **24**, 1117–1130, <https://doi.org/10.1175/JTECH2016.1>.
- Lueck, R. G., 1990: Thermal inertia of conductivity cells: Theory. *J. Atmos. Oceanic Technol.*, **7**, 741–755, [https://doi.org/10.1175/1520-0426\(1990\)007<0741:TIOCCT>2.0.CO;2](https://doi.org/10.1175/1520-0426(1990)007<0741:TIOCCT>2.0.CO;2).
- , and J. J. Picklo, 1990: Thermal inertia of conductivity cells: Observations with a Sea-Bird cell. *J. Atmos. Oceanic Technol.*, **7**, 756–768, [https://doi.org/10.1175/1520-0426\(1990\)007<0756:TIOCCO>2.0.CO;2](https://doi.org/10.1175/1520-0426(1990)007<0756:TIOCCO>2.0.CO;2).
- Martini, K. I., D. J. Murphy, R. W. Schmitt, and N. G. Larson, 2019: Corrections for pumped SBE 41CP CTDs determined from stratified tank experiments. *J. Atmos. Oceanic Technol.*, **36**, 733–744, <https://doi.org/10.1175/JTECH-D-18-0050.1>.
- Morison, J., R. Andersen, N. Larson, E. D'Asaro, and T. Boyd, 1994: The correction for thermal-lag effects in Sea-Bird CTD data. *J. Atmos. Oceanic Technol.*, **11**, 1151–1164, [https://doi.org/10.1175/1520-0426\(1994\)011<1151:TCFTLE>2.0.CO;2](https://doi.org/10.1175/1520-0426(1994)011<1151:TCFTLE>2.0.CO;2).
- Nezlin, N. P., and Coauthors, 2020: Accuracy and long-term stability assessment of inductive conductivity cell measurements on Argo floats. *J. Atmos. Oceanic Technol.*, **37**, 2209–2223, <https://doi.org/10.1175/JTECH-D-20-0058.1>.
- Owens, W. B., and A. P. Wong, 2009: An improved calibration method for the drift of the conductivity sensor on autonomous CTD profiling floats by  $\theta - S$  climatology. *Deep-Sea Res. I*, **56**, 450–457, <https://doi.org/10.1016/j.dsr.2008.09.008>.
- RBR, 2021: Argo float WMO5906299: Analysis of fresh salinity anomalies. RBR Tech. Rep., 3 pp., [https://oem.rbr-global.com/floats/files/5898249/46235845/1/1624471832000/0011136revA+Argo+float+WMO5906299\\_+Analysis+of+fresh+salinity+anomalies.pdf](https://oem.rbr-global.com/floats/files/5898249/46235845/1/1624471832000/0011136revA+Argo+float+WMO5906299_+Analysis+of+fresh+salinity+anomalies.pdf).
- Rees, C., and M. McMahon, 2019: RV Investigator hydrochemistry data processing report. CSIRO Tech. Rep., 10 pp.
- Roemmich, D., and Coauthors, 2019: On the future of Argo: A global, full-depth, multi-disciplinary array. *Front. Mar. Sci.*, **6**, 439, <https://doi.org/10.3389/fmars.2019.00439>.
- Sanabia, E. R., and S. R. Jayne, 2020: Ocean observations under two major hurricanes: Evolution of the response across the storm wakes. *AGU Adv.*, **1**, e2019AV000161, <https://doi.org/10.1029/2019AV000161>.
- Schmitt, R. W., R. C. Millard, J. M. Toole, and W. D. Wellwood, 2005: A double-diffusive interface tank for dynamic-response studies. *J. Mar. Res.*, **63**, 263–289, <https://doi.org/10.1357/0022240053693842>.
- Sea-Bird, 2013: Compressibility compensations of Sea-Bird conductivity sensors. Sea-Bird Application Note 10, 3 pp., <http://www.seabird.com/application-notes>.
- Ullman, D. S., and D. Hebert, 2014: Processing of underway CTD data. *J. Atmos. Oceanic Technol.*, **31**, 984–998, <https://doi.org/10.1175/JTECH-D-13-00200.1>.
- Wong, A. P. S., G. C. Johnson, and W. B. Owens, 2003: Delayed-mode calibration of autonomous CTD profiling float salinity data by  $\theta - S$  climatology. *J. Atmos. Oceanic Technol.*, **20**, 308–318, [https://doi.org/10.1175/1520-0426\(2003\)020<0308:DMCOAC>2.0.CO;2](https://doi.org/10.1175/1520-0426(2003)020<0308:DMCOAC>2.0.CO;2).
- , and Coauthors, 2020: Argo data 1999–2019: Two million temperature-salinity profiles and subsurface velocity observations from a global array of profiling floats. *Front. Mar. Sci.*, **7**, 700, <https://doi.org/10.3389/fmars.2020.00700>.